



## Evaluating states in trapped ions with local correlation between internal and motional degrees of freedom

Silpa Muralidharan <sup>1,\*</sup>, Ryutaro Ohira,<sup>1,2</sup> Shota Kume,<sup>1</sup> and Kenji Toyoda <sup>2,†</sup>

<sup>1</sup>*Graduate School of Engineering Science, Osaka University, 1-3 Machikaneyama, Toyonaka, Osaka 560-8531, Japan*

<sup>2</sup>*Center for Quantum Information and Quantum Biology, Osaka University, 1-2 Machikaneyama, Toyonaka, Osaka 560-0043, Japan*



(Received 9 May 2021; revised 3 November 2021; accepted 19 November 2021; published 6 December 2021)

We propose and demonstrate a scalable scheme for the simultaneous determination of internal and motional states in trapped ions with single-site resolution. The scheme is applied to the study of polaritonic excitations in the Jaynes-Cummings-Hubbard model with trapped ions, in which the internal and motional states of the ions are strongly correlated. We observe quantum phase crossovers of polaritonic excitations in two ions by directly evaluating their variances per ion site. Our work establishes an essential technological method for large-scale quantum simulations of polaritonic systems.

DOI: [10.1103/PhysRevA.104.062410](https://doi.org/10.1103/PhysRevA.104.062410)

### I. INTRODUCTION

Quantum simulations allow us to study the properties of many-body quantum systems that are hard to investigate with classical computers [1]. A promising platform for realizing quantum simulations is a system of trapped ions [2,3]. Trapped ions have advantages over other systems from such perspectives as ease of preparation and control, and we can address individual particles with little perturbation to neighboring particles.

The Jaynes-Cummings (JC) model describes the atom-field interaction in a combined system of a two-level atom and a quantized electric-field mode [4]. An interconnected array of two-level atoms interacting with quantized wave modes is known as the Jaynes-Cummings-Hubbard (JCH) model, and related systems of coupled cavity arrays have been extensively investigated [5–11].

The JCH model can be realized with arrays of cavity QED systems [12,13] and of circuit QED systems [14–18], as well as systems of trapped ions [10,19–23]. These systems can be flexibly controlled with sets of system parameters. Therefore, they can be considered to be attractive systems for studying quantum many-body phenomena.

In the JCH model, quasiparticles called polaritons play an essential role. Each polariton is represented as the superposition of an internal excitation and a photon or a motional excitation (phonon). Polaritons are well-defined particles in the JCH model and their total number is conserved. The implications for understanding the JCH model are apparent in the quantum phase transition of a JCH system between the Mott-insulator (MI) and superfluid (SF) phases, which are characterized by a drastic change in the polariton-number variance per site [7].

In the case of the JCH model with trapped ions [19], each polariton is a correlated combination of an internal excita-

tion and a vibrational quantum (local phonon [21,22,24–31]). Therefore, by detecting the internal and motional states, the states of polaritons can be precisely evaluated. It is not easy to directly measure the motional states and they should instead first be mapped to the internal states to be detected by, e.g., state-dependent fluorescence detection. However, this process destroys the internal states. The internal and motional states cannot be simultaneously determined even if we measure the former and the latter consecutively in this order since the measurement of the internal states with fluorescence detection may destroy the motional states due to photon recoil during several fluorescence cycles.

One approach to address this is a conditional measurement method [19,32] using levels in such ions as  $^{40}\text{Ca}^+$ , which has a metastable state. In this method, a random guess of the internal states (the ground state  $|g\rangle$  or the metastable state  $|e\rangle$ ) of a particular ion is first made. If the guess is made for the  $|g\rangle$  or  $|e\rangle$  state, a carrier  $\pi$  pulse or no pulse, respectively, is applied to the  $|g\rangle\text{--}|e\rangle$  transition. Then, laser light resonant to the transition between  $|g\rangle$  and a short-lived excited state is exposed to the ions. If the ion scatters fluorescence at this point, the initial guess was wrong and the measurement result is discarded. Otherwise, the initial guess was right and the internal state is subsequently transferred back to the  $|g\rangle$  state. An analysis of the motional states using a blue-sideband (BSB) Rabi oscillation is then performed. Fourier analyses on a series of these results give information on the motional states and the internal states that correspond to the initial guesses. This combined information retains the local correlation between the internal and motional states in the states of interest. This method can be applied to the case of a single ion.

In the case of an ion chain, the concept of local vibrational modes (local phonons) becomes approximate. Each mode can be coupled with those in different ion sites through Coulomb couplings. When a particular ion site is heated due to photon recoils during fluorescence cycles, the heat is transferred to different ion sites and eventually the motional states at those sites may be destroyed (mutual heating among ion sites).

\*u928298g@ecs.osaka-u.ac.jp

†toyoda@qiqb.osaka-u.ac.jp

In this article, we demonstrate the measurement of local motional states conditioned on the internal states by shelving part of the ions to a long-lived internal state. In this method, fluorescence cycles are not used to determine the internal states, and the probability amplitudes that are of no interest are simply hidden in the auxiliary long-lived internal state. Therefore, this method does not suffer from mutual heating among ion sites as explained above, and is applicable to the measurement of local motional states in a multi-ion crystal. In this work, this method is applied to determine the polariton number and its variance in the JCH model while the system parameters are changed. The method is scalable with respect to the number of ion sites, i.e., the same time sequence can be used in principle for an arbitrary number of ions in the chain.

## II. JCH MODEL

The JC model [4] was initially proposed by Jaynes and Cummings in 1963. It is a quantum optics model that describes the interaction of a two-level atom with a single quantized mode of an optical cavity electromagnetic field. The model is widely used in such fields as cavity QED and circuit QED. The Hamiltonian for the JC model is given as

$$H_{\text{JC}} = \hbar\omega\hat{a}^\dagger\hat{a} + \frac{1}{2}\hbar\omega_0\hat{\sigma}_z + \hbar g(\hat{\sigma}_+\hat{a} + \hat{\sigma}_-\hat{a}^\dagger), \quad (1)$$

where  $\omega$  is the oscillation frequency of the electromagnetic field,  $\hat{a}^\dagger$  and  $\hat{a}$  are the creation and annihilation operators, respectively, for the quantized mode of the electromagnetic field,  $\omega_0$  is the resonance frequency of the two-level atom,  $\hat{\sigma}_z$  is the Pauli operator in the  $z$  direction,  $g$  is the JC coupling coefficient, and  $\hat{\sigma}_+$  and  $\hat{\sigma}_-$  are the atomic raising and lowering operators, respectively. This model introduces superposition states corresponding to dressed atoms or polaritons and a semi-infinite series of eigenenergies called the JC ladder [4]. It leads to such phenomena as a vacuum-field Rabi oscillation or collapses and revivals of atomic oscillations. The analogy between a cavity QED system and a trapped-ion system leads to implementing the JC model in trapped-ion experiments for quantum information processing.

When trapped ions in an ion chain with relatively tight confinement along the radial directions [24] are used and optical fields resonant to the red-sideband (RSB) transitions are applied, the two-level systems in the ions interacting with radial local phonons can be considered as an interconnected array of JC systems, which can be described with the JCH model. The Hamiltonian for the JCH model in a system of two trapped ions is given as [19]

$$H_{\text{JCH}} = \hbar\frac{\kappa}{2}(\hat{a}_1^\dagger\hat{a}_2 + \hat{a}_1\hat{a}_2^\dagger) + \hbar\Delta \sum_{j=1,2} |e_j\rangle \langle e_j| + \hbar g \sum_{j=1,2} (\hat{a}_j^\dagger\hat{\sigma}_j^- + \hat{a}_j\hat{\sigma}_j^+), \quad (2)$$

where  $\kappa$  is the hopping rate of the radial local phonons,  $\hat{a}_j^\dagger$  and  $\hat{a}_j$  are the creation and annihilation operators, respectively, for phonons at the  $j$ th ion,  $\Delta$  is the amount of detuning of the optical field from the RSB transition,  $|e_j\rangle$  is the internal excited state in the  $j$ th ion, and  $\sigma_j^+ \equiv |e_j\rangle \langle g_j|$  and  $\sigma_j^- \equiv |g_j\rangle \langle e_j|$  are the raising and lowering operators, respectively, for the internal states in the  $j$ th ion, where  $|g_j\rangle$  is the internal ground

state in the  $j$ th ion. In this JCH system, quantum phase transitions between the MI and SF phases are expected to occur [5,7]. A quantum phase transition is similar to a classical phase transition, while the cause of the transition is directly related to quantum fluctuations instead of such parameters as pressure or temperature. In the case of a small number of involved particles, as in this work with two ions, quantum phase transitions can be more adequately termed as “quantum phase crossovers,” implying the finite nature of the system as well as nonabrupt transitions.

## III. MI-TO-SF QUANTUM PHASE CROSSOVERS IN THE JCH MODEL

In the JCH model, a quantum phase crossover from the MI phase to the SF phase in a trapped-ion chain is realized by the adiabatic transfer process [5,6]. Here, we consider that the ions are prepared in  $|\psi_{\text{MI}}\rangle = |e_1\rangle |e_2\rangle |0\rangle_1 |0\rangle_2$ . This state corresponds to a ground state, the MI state, in which the excitations are localized. The parameters  $\Delta$  and  $g$  can be changed by varying the frequency and amplitude of the laser, respectively. We linearly sweep  $\Delta$  from a negative value to a positive one and change the amplitude (and hence  $g$ ) following a Gaussian shape. In this case, the Hamiltonian changes time dependently and an adiabatic transfer is induced [33]. At the final stage of this transfer, a ground state called the SF phase is created, which has the form  $|\psi_{\text{SF}}\rangle = |g_1\rangle |g_2\rangle \otimes [(1/\sqrt{2})|1\rangle_1 |1\rangle_2 - (1/2)|2\rangle_1 |0\rangle_2 - (1/2)|0\rangle_1 |2\rangle_2]$  [34]. In the intermediate region of the adiabatic transfer, polaritonic MI and SF phases exist.

In an analogy to second-order phase transitions in statistical physics, quantum phase crossovers in the current system can be understood by the emergence and disappearance of certain ordered phases. The MI states are considered to have an order in the excitation (polariton) number per site, in close analogy to the Bose-Hubbard systems [35,36]. The SF states in this system are believed to have coherence among multiple sites. In the case of two ions, the phonon and polaritonic SF states can be represented as superpositions of product states over multiple sites [34]. Although it is not straightforward to define an order parameter that embodies the coherence among multiple sites, the order in the polariton number per site can be readily defined.

Angelakis *et al.* proposed using the polariton-number variance per site to determine the different phases of the system [7]; it tends to be zero for the MI phase, which has perfect number order, while it takes finite values for the SF phase. Accordingly, we use the variance for the total excitation number (polariton number) per site to determine quantum phase crossovers in the JCH model. Other excitation-number variances (atomic and phonon) can be used for purposes such as classifying the ground states of the system.

The variance for the total excitation number per site (total variance) is given by  $\Delta\hat{N}_j^2 \equiv \langle \hat{N}_j^2 \rangle - \langle \hat{N}_j \rangle^2$ , where  $\hat{N}_j = |e_j\rangle \langle e_j| + \hat{a}_j^\dagger\hat{a}_j$ . The variance for the atomic excitation number per site (atomic variance) is given by  $\Delta\hat{N}_{a,j}^2 \equiv \langle \hat{N}_{a,j}^2 \rangle - \langle \hat{N}_{a,j} \rangle^2$ , where  $\hat{N}_{a,j} = |e_j\rangle \langle e_j|$ . This helps to identify polaritons. Additionally, the variance for the phonon number per site (phonon variance) is defined as  $\Delta\hat{N}_{p,j}^2 \equiv \langle \hat{N}_{p,j}^2 \rangle - \langle \hat{N}_{p,j} \rangle^2$ ,

TABLE I. Variances and classes of the ground states.

	$\Delta N_{a,k} = 0$	$\Delta N_{a,k} \neq 0$
$\Delta N_{i,k} = 0$	Atomic MI	Polaritonic MI
$\Delta N_{i,k} \neq 0$	Phonon SF	Polaritonic SF

where  $\hat{N}_{p,j} = \hat{a}_j^\dagger \hat{a}_j$ . This follows an increasing trend similar to that for the total variance in MI-to-SF quantum phase crossovers, while its detailed behavior in the intermediate region is different from that for the total variance. The values for the total and atomic variances and the corresponding classes of the ground states are summarized in Table I.

#### IV. CONDITIONAL MEASUREMENT OF INTERNAL AND MOTIONAL STATES

The time sequences for the conditional-measurement scheme are given in Figs. 1(a)–1(c). The overall time sequence is given in Fig. 1(a). The third section labeled as “Meas.” [Figs. 1(b) or 1(c)] in the time sequence corresponds to the conditional measurement, which is performed in two different ways: one is conditioned on  $|g\rangle$  [Fig. 1(b)] and the other on  $|e\rangle$  [Fig. 1(c)]. These two cases will be explained in more details later. Figures 1(d)–1(f) shows the levels used for the conditional-measurement scheme, as well as the relevant probability amplitudes (green text) before the conditional measurement [Fig. 1(d)], before the measurement of BSB Rabi oscillations conditioned on  $|g\rangle$  [Fig. 1(e)], and before that conditioned on  $|e\rangle$  [Fig. 1(f)].

In the scheme proposed here, an auxiliary long-lived internal state (a sublevel in the Zeeman manifold of the excited state, denoted as  $|a\rangle$ ) is used. The levels in the internal two-

level system  $\{|g\rangle, |e\rangle\}$  are connected by a carrier transition [denoted as “Carrier” in Figs. 1(d)–1(f)], while the internal ground state  $|g\rangle$  and the auxiliary state  $|a\rangle$  are connected by another carrier transition [denoted as “Shelving” in Figs. 1(d)–1(f)]. We assume that the motional states can be treated as a set of local vibrational modes. This is an approximate picture, which is valid as long as the sideband Rabi frequencies used for the analysis of the motional states during the conditional measurements are much larger than the intersite coupling rates of the motional states.

In the time sequence involving conditional measurements, at first the system is cooled to the vibrational ground state and an optical pumping to a particular Zeeman sublevel in the internal ground-state manifold is performed [“State prep.” in Fig. 1(a)]. Then a quantum simulation (equivalent to the adiabatic transfer mentioned above) and a conditional measurement are performed.

The conditional measurement is performed in two different ways: one is conditioned on  $|g\rangle$  [Fig. 1(b)] and the other on  $|e\rangle$  [Fig. 1(c)]. We explain these two cases using a formulation, assuming a chain of  $N$  ions, where each ion has three internal states and an associated local vibrational mode. The Coulomb couplings between different ion sites are ignored temporarily for simplicity. The state of the  $i$ th ion is expressed as

$$|\psi_i\rangle = \sum_{x=g,e} |\psi_x\rangle_i, \quad (3)$$

where

$$|\psi_g\rangle_i = \sum_{n=0}^m C_{g,n} |g, n\rangle_i, \quad (4)$$

$$|\psi_e\rangle_i = \sum_{n=0}^m C_{e,n} |e, n\rangle_i. \quad (4)$$

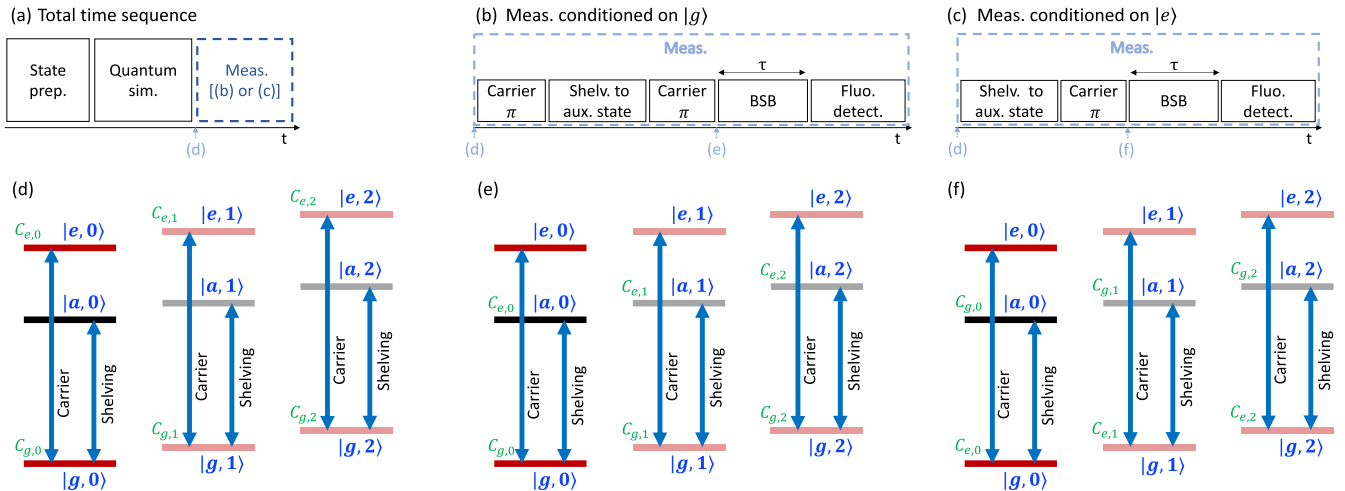


FIG. 1. (a)–(c) Time sequences for conditional measurements and (d)–(f) level scheme with probability amplitudes. (a) Total time sequence. First, the initial state is prepared. Then a quantum simulation (an adiabatic transfer) and a conditional measurement are performed. (b) Time sequence for a measurement conditioned on  $|g\rangle$ .  $\tau$  is the variable length of the BSB pulse, which is swept to obtain the BSB oscillation signals. (c) Time sequence for a measurement conditioned on  $|e\rangle$ .  $\tau$  is a variable length similar to the one above. (d) Level scheme and probability amplitudes associated with the levels before a conditional measurement. The time corresponding to this is indicated in (a)–(c) with a dashed arrow and a text “(d)” in thin blue. (e) Levels and probability amplitudes after conditioning the system to  $|g\rangle$ . The time corresponding to this is indicated in (b) with a dashed arrow and a text “(e)” in thin blue. (f) Levels and probability amplitudes after conditioning the system to  $|e\rangle$ . The time corresponding to this is indicated in (c) with a dashed arrow and a text “(f)” in thin blue.

Here,  $|g, n\rangle_i \equiv |g\rangle_i |n\rangle_i$  and  $|e, n\rangle_i \equiv |e\rangle_i |n\rangle_i$ , where  $n$  is the phonon number. It is assumed that the maximum number of phonons in each vibrational mode is  $m$ . The coefficients  $C_{g,n}$  and  $C_{e,n}$  are probability amplitudes satisfying  $\sum_{n=0}^m (|C_{g,n}|^2 + |C_{e,n}|^2) = 1$ . [See Fig. 1(d) for the initial arrangement of the probability amplitudes.]

As a preparation step for performing an analysis of the motional state in the conditional-measurement scheme, we transfer the population in either  $|g\rangle$  or  $|e\rangle$  to a long-lived auxiliary state  $|a\rangle$ , depending on which state we want to analyze.

To analyze the probabilities associated with  $|g\rangle$ , we use the time sequence given in Fig. 1(b). We first apply a  $\pi$  pulse resonant to the transition  $|g\rangle \leftrightarrow |e\rangle$ . This is followed by a  $\pi$  pulse resonant to the  $|g\rangle \leftrightarrow |a\rangle$  transition and a second  $\pi$  pulse resonant to the  $|g\rangle \leftrightarrow |e\rangle$  transition. These three pulses effectively shelve populations originally in  $|e\rangle$  to  $|a\rangle$ , and keep those originally in  $|g\rangle$  in the same state. The state after the application of these pulses is represented as

$$|\psi_i\rangle = \sum_{x=g,a} |\psi_x\rangle_i, \quad (5)$$

where

$$\begin{aligned} |\psi_g\rangle_i &= \sum_{n=0}^m C_{g,n} |g, n\rangle_i, \\ |\psi_a\rangle_i &= \sum_{n=0}^m C_{e,n} |a, n\rangle_i. \end{aligned} \quad (6)$$

[See Fig. 1(e) for the arrangement of the probability amplitudes in this case.]

By applying a BSB pulse to this state, whose variable length  $\tau$  is swept from 0 to a certain time, Rabi oscillations between  $|g, n\rangle \leftrightarrow |e, n+1\rangle$  can be observed. By performing Fourier analysis on the results, it is possible to deduce the probabilities  $|C_{g,n}|^2$  originally associated with  $|g\rangle$ .

To measure the probabilities associated with  $|e\rangle$ , we use a slightly different time sequence, as shown in Fig. 1(c). In this case, the first  $\pi$  pulse used in the previous case is omitted, while the following sequence is used as is. Before applying the BSB pulse, the state is similar to Eq. (6), where  $C_{g,n}$  and  $C_{e,n}$  are replaced with each other. [See Fig. 1(f) for the arrangement of the probability amplitudes in this case.] By applying a BSB pulse with a variable length  $\tau$  and performing Fourier analysis on the result, the probabilities  $|C_{e,n}|^2$  originally associated with  $|e\rangle$  can be obtained.

Collecting the results of these measurements, it is possible to evaluate the internal and motional states. For example, the probability for states with  $k$  polaritons is given as

$$P_{\text{pol}}^k = \begin{cases} |C_{g,k}|^2 & (k = 0) \\ |C_{g,k}|^2 + |C_{e,k-1}|^2 & (k \geq 1). \end{cases} \quad (7)$$

We should mention the effective fraction of measurements in this scheme. In contrast to the conditional-measurement schemes used previously [19,32], which involve a dedicated measurement of the internal state in advance of the measurement of the motional state in each sequence, our scheme uses shelving of the probability amplitudes that are of no interest to an auxiliary internal state. This helps avoid unwanted effects of heating from adjacent ion sites during fluorescence cycles,

and omits post-selections. However, the effective amount of information acquired is reduced in this scheme due to the fact that some of the probability amplitudes are hidden in the auxiliary level. In this sense, this scheme is not superior to those methods that use post-selections [19,32]. The overall loss of information, on average, is estimated to be 50%. For example, if we perform 100 measurement trials conditioned on  $|g\rangle$  and the same number of trials conditioned on  $|e\rangle$ , the average net amount of the effective trials would be 100 in total, and the respective ratio of the effective trials over the total number may differ between  $|g\rangle$  and  $|e\rangle$ , depending on the internal-state population. The effective fraction of 50% does not depend on the number of ions involved. Therefore, it can be asserted that this scheme is scalable with respect to the number of ions in this sense.

This loss of information manifests in the observed results as a reduction in the contrasts in the BSB Rabi oscillation signals and associated offsets corresponding to the populations hidden to the long-lived auxiliary state. (The populations in the auxiliary state cannot be distinguished from those in the excited state in our case.) The contrast in the results conditioned on  $|g\rangle$  or  $|e\rangle$  should be proportional to the population in that state before the conditional-measurement sequence. Therefore, a fitting process should be adapted to such signals with different contrasts and offsets. We will discuss this in Sec. VII A.

## V. EXPERIMENTAL PROCEDURE

Two  $^{40}\text{Ca}^+$  ions are trapped in a linear Paul trap. An rf voltage of 23 MHz is applied for radial confinement. An rf quadrupole electric field with a frequency of 23 MHz is applied for radial confinement, and a dc potential is applied for axial confinement. The secular frequencies are  $(\omega_x, \omega_y, \omega_z)/2\pi = (2.6, 2.4, 0.15)$  MHz. The distance between the two ions is 20  $\mu\text{m}$  and the hopping rate of local phonons [24,37] is 3.8 kHz. The ions are first cooled by Doppler cooling along all directions, and then their vibrational motion along the two radial directions ( $x$  and  $y$ ) is reduced to the ground state by sideband cooling [38,39]. Doppler cooling is realized with 397-nm ( $S_{1/2}-P_{1/2}$ ) and 866-nm ( $D_{3/2}-P_{3/2}$ ) laser beams and sideband cooling is realized with 729-nm ( $S_{1/2}-D_{5/2}$ ) and 854-nm ( $D_{5/2}-P_{3/2}$ ) laser beams. Sideband cooling is performed with a repetition of a pulse section 20 times, in each of which 729- and 854-nm pulses are simultaneously applied for 400  $\mu\text{s}$ . The ions are intermittently optically pumped to  $S_{1/2}$  by a 397-nm beam with  $\sigma^-$  polarization before, between, and after the pulse sections for sideband cooling. The final vibrational quantum numbers along the radial directions after sideband cooling are  $\{\bar{n}_x, \bar{n}_y\} \sim \{0.2, 0.1\}$ .

The  $y$  radial direction in the ion crystal is used for the motional degree of interest in this work. There are two collective modes in this direction, i.e., the center-of-mass (COM) and rocking modes, which are separated from each other in frequency by a spacing similar to the hopping rate. The heating rate for the  $y$  direction is estimated to be  $\sim 5$  quanta/s [30].

Excitation beams at 729 nm for  $S_{1/2}-D_{5/2}$  are used to induce JC coupling, as well as to prepare and analyze the internal and motional states. The level scheme of  $^{40}\text{Ca}^+$  relevant for the manipulation of the internal and motional

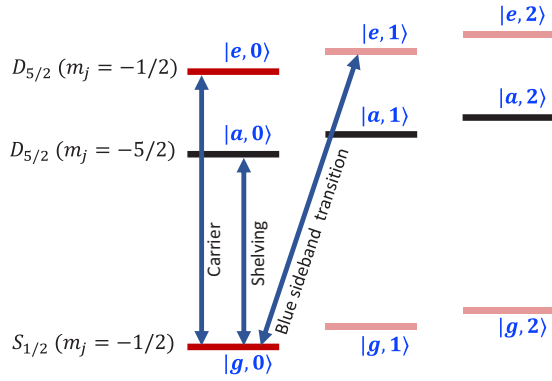


FIG. 2. Level scheme for a trapped  $^{40}\text{Ca}^+$  with internal ground ( $|g, n\rangle$ ), excited ( $|e, n\rangle$ ), and auxiliary ( $|a, n\rangle$ ) states, where  $n$  represents the motional quantum number in a local vibrational mode.

states is shown in Fig. 2. (In this figure, the motional state is assumed to be that of a local vibrational mode in view of applying this to the measurement scheme.) We use  $S_{1/2}(m_j = -1/2)$ ,  $D_{5/2}(m_j = -1/2)$ , and  $D_{5/2}(m_j = -5/2)$  as the internal ground ( $|g\rangle$ ), excited ( $|e\rangle$ ), and auxiliary ( $|a\rangle$ ) states, respectively. Figure 2 also shows the quantum numbers for the local vibrational mode as the second arguments for the basis kets.

The excitation beams at 729 nm are individually applied to each of the two ions. The relative intensities of the beams are adjusted to optimize equal illumination of the two ions, by balancing the maximum Rabi frequencies between the two ions.

The fluctuations in the radial secular frequencies are reduced by introducing a feedback-control system for the rf amplitude [40].

The internal state of the two ions is determined by illuminating them with lasers at 397 and 866 nm and by detecting fluorescence photons with a photomultiplier tube or an electron multiplying charge-coupled-device camera.

In the quantum simulation of the JCH model, first the system is prepared in the atomic MI state ( $|\psi_{\text{MI}}\rangle = |e_1\rangle|e_2\rangle|0\rangle_1|0\rangle_2$ ) by applying a carrier  $\pi$  pulse at 729 nm after sideband cooling. Then an adiabatic transfer is performed, with a duration of typically  $960 \mu\text{s}$ . The duration is determined to satisfy the adiabaticity in the internal states, while the adiabaticity in the motional state is not fully satisfied (discussed in Sec. VIIC). The internal state during this adiabatic transfer can be detected by truncating it and by illuminating the ions with the lasers at 397 and 866 nm. A conditional measurement, as explained above, involving the excitation of the BSB transition, can also be performed by truncating the adiabatic transfer.

## VI. MEASUREMENT OF INTERNAL-STATE POPULATIONS

The results of internal-state measurements from 0 to  $960 \mu\text{s}$  are shown in Fig. 3. The measured population (blue circles with error bars) and a numerical simulation for the population (red dashed curve) are shown in Fig. 3(a). The time dependence of the parameters used in the numerical

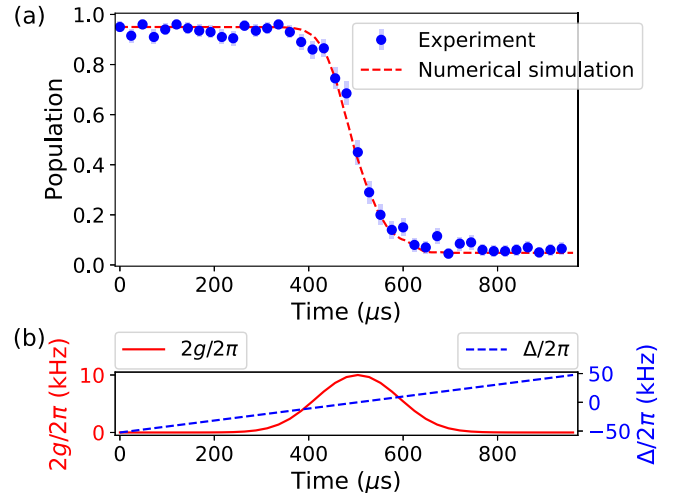


FIG. 3. (a) Experimentally observed adiabatic-transfer curve (blue circles and error bars) and numerically simulated results (red dashed curve). Each experimental point is the average of 100 experiments, and the error is calculated by assuming a binomial distribution. (b) Time dependence of the parameters for the optical pulse assumed in the numerical simulation in (a):  $g$  (JC-coupling constant) divided by  $\pi$  (red solid curve) and  $\Delta$  (detuning) divided by  $2\pi$  (blue dashed curve) for the numerical simulation.

simulation in Fig. 3(a) is plotted in Fig. 3(b). The conditions for the numerical simulation are summarized as follows. The hopping rate  $\kappa/2\pi$  is 3.8 kHz.  $2g/2\pi$  is swept in a Gaussian form with a maximum value of 10.0 kHz.  $\Delta/2\pi$  is varied from  $-50$  to  $50$  kHz during a time of  $960 \mu\text{s}$ . The Lindblad master equation [41] is used for the numerical simulation, in which transverse relaxation for the BSB transition, for example due to fluctuations of the sideband resonance frequencies, is taken into account by using  $\gamma_{\text{T}} = 2\pi \times 0.19$  kHz as the rate. The initial populations in the internal states are set to be 0.95 in  $|e\rangle$  and 0.05 in  $|g\rangle$  [42].

The greater than zero final population can be explained mainly by the effect of transverse relaxation. In our estimation, the effect of diabaticity is not significant for this particular case.

## VII. CONDITIONAL MEASUREMENTS AND EVALUATION OF VARIANCES

### A. Evaluation of populations from fitting

In performing the conditional measurements to evaluate the variances, we applied the two different time sequences given in Figs. 1(b) and 1(c) in separate experimental runs, and the BSB Rabi oscillations in both cases were measured. By analyzing the Rabi oscillation results in both cases via fitting with model functions and by combining the acquired information, the state populations were inferred and the variances were then evaluated.

The atomic variance can be estimated if the internal-state population is known. For the particular conditional measurements in this work, we used the first points of the BSB Rabi oscillations, for which no BSB pulse of a finite length is applied, to infer the population in the internal states. These

are equivalent to the internal-state populations just before the application of the BSB pulses in Figs. 1(b) and 1(c). Those populations are denoted as  $P_g$  and  $P_e$  for the ground and excited states, respectively. Here, we assume that the system is symmetric with respect to the permutation of the two ions, and hence that the populations for the two ions are identical to each other.

For the estimation of the phonon and total variances, especially for the latter, the information obtained from conditional measurements is fully exploited. The obtained BSB Rabi oscillation signals are analyzed by fitting the obtained results with model functions derived from those used in standard analyses on sideband Rabi oscillations [43],

$$\Pi_e(t) = \frac{1}{2}a \left[ 1 + \sum_{n=0}^m \tilde{P}_n \cos^2(\Omega_{n,n+1}t/2) e^{-\gamma_R t} \right] + (1-a).$$

Here,  $\Pi_e(t)$  is the time-dependent excited-state population during the BSB excitation,  $m$  is the maximum Fock-state quantum number that is assumed,  $\tilde{P}_n$  is the population in each motional Fock state before the BSB excitation,  $\Omega_{n,n+1} \equiv \eta\Omega_0\sqrt{n+1}$  is the BSB Rabi frequency ( $\eta$  is the Lamb Dicke factor and  $\Omega_0$  is the resonant Rabi frequency for an ion without motion; the terms of higher orders in  $\eta$  are ignored here), and  $\gamma_R$  is the common relaxation rate reflecting decoherence and dephasing processes in sideband Rabi oscillations [44].  $a$  ( $0 \leq a \leq 1$ ) is a factor that takes into account the reduction of contrasts and the associated offsets as discussed above. Here,  $a$  is determined from the estimated internal-state populations, as explained in the last paragraph.

In the actual fitting process, the maximum Fock-state quantum number  $m$  is set to 2 [45]. The base Rabi frequency  $\Omega_{0,1}$  and  $(\tilde{P}_0, \tilde{P}_1, \tilde{P}_2)$  ( $\tilde{P}_0 + \tilde{P}_1 + \tilde{P}_2 = 1$ ) for each result, as well as the overall relaxation rate  $\gamma_R$ , are determined iteratively. First, we use empirically known fixed values of  $(\tilde{P}_0, \tilde{P}_1, \tilde{P}_2)$  for each result and perform a fitting of all the results with the least-squares method to determine  $\Omega_{0,1}$  for each result and  $\gamma_R$  (the latter is determined by finding the value that gives the minimum value for the sum of the chi squares in fitting of all the results). We then treat these values as fixed values and repeat the fitting process, thereby determining the refined values for  $(\tilde{P}_0, \tilde{P}_1, \tilde{P}_2)$ . This whole process is repeated multiple times to obtain the final values for  $(\tilde{P}_0, \tilde{P}_1, \tilde{P}_2)$ . By multiplying  $a$  by these values, the actual populations in the combined internal and motional state basis states are determined. For example, in the case for conditioning on  $|g\rangle$  or  $|e\rangle$ , we obtain  $(P_{g,0}, P_{g,1}, P_{g,2})$  or  $(P_{e,0}, P_{e,1}, P_{e,2})$ , respectively, which is equal to  $(a\tilde{P}_0, a\tilde{P}_1, a\tilde{P}_2)$ . Here,  $P_{x,n} \equiv |C_{x,n}|^2$  ( $x = g, e$ ) is the population in each combined internal and motional basis state  $|x, n\rangle$ . We also evaluate the error for each of the populations, which is calculated as that propagating from the parameter errors in the fitting process.

### B. Evaluation of variances

The variances defined in Sec. III, including the total, atomic, and phonon variances, are obtained from the combined information acquired in both the cases conditioned on  $|g\rangle$  and  $|e\rangle$ . In this section, we present the method to calculate the variances using populations based on the method in the

previous section. As mentioned above, we assume that the system is symmetric with respect to the permutation of the two ions, and omit the subscript  $j = 1, 2$  representing the index for the ion number in the following. The atomic variance is obtained as

$$\begin{aligned} (\Delta\hat{N}_a)^2 &= \text{tr}(\rho\hat{N}_a^2) - \text{tr}(\rho\hat{N}_a)^2 \\ &= P_e - P_e^2, \end{aligned} \quad (8)$$

where  $\rho$  is the density operator for the total system and  $P_e = \langle e | \rho | e \rangle$  (this is equal to  $\sum_{n=0}^2 P_{e,n}$  when the phonon number  $n$  is limited to  $0 \leq n \leq 2$ ). The phonon variance is obtained as

$$\begin{aligned} (\Delta\hat{N}_p)^2 &\simeq \sum_{n=0}^2 n^2 P_n - \left( \sum_{n=0}^2 n P_n \right)^2 \\ &= P_1 + 4P_2 - (P_1 + 2P_2)^2, \end{aligned} \quad (9)$$

where  $P_n \equiv P_{g,n} + P_{e,n}$  ( $n = 0, 1, 2$ ). The total variance can be expressed as

$$\begin{aligned} (\Delta\hat{N})^2 &= \langle (\hat{N}_a + \hat{N}_p)^2 \rangle - \langle \hat{N}_a + \hat{N}_p \rangle^2 \\ &= (\langle \hat{N}_a^2 \rangle - \langle \hat{N}_a \rangle^2) + (\langle \hat{N}_p^2 \rangle - \langle \hat{N}_p \rangle^2) \\ &\quad + 2(\langle \hat{N}_a \hat{N}_p \rangle - \langle \hat{N}_a \rangle \langle \hat{N}_p \rangle) \\ &= (\Delta\hat{N}_a)^2 + (\Delta\hat{N}_p)^2 + 2\overline{\text{Cov}}(\hat{N}_a, \hat{N}_p), \end{aligned} \quad (10)$$

where

$$\begin{aligned} \overline{\text{Cov}}(\hat{N}_a, \hat{N}_p) &\equiv \langle \hat{N}_a \hat{N}_p \rangle - \langle \hat{N}_a \rangle \langle \hat{N}_p \rangle \\ &\simeq \sum_{n=0}^2 n P_{e,n} - P_e \sum_{n=0}^2 n P_n \\ &= P_{e,1} + 2P_{e,2} - P_e(P_1 + 2P_2) \end{aligned} \quad (11)$$

is the covariance between the two quantum mechanical observables, the atomic excitation number, and the phonon number.

Using Eqs. (8)–(11), the total variance can be obtained as

$$\begin{aligned} (\Delta\hat{N})^2 &\simeq P_e - P_e^2 + P_1 + 4P_2 - (P_1 + 2P_2)^2 \\ &\quad + 2[P_{e,1} + 2P_{e,2} - P_e(P_1 + 2P_2)]. \end{aligned} \quad (12)$$

We also evaluate the error for each of the variances, which is calculated as that propagating from those of the evaluated values for the populations [46]. See the Appendix A for the estimation of errors in the variances.

### C. Experimental results

The experimental Rabi oscillation results measured after truncating the adiabatic transfer at certain selected points in time (48, 432, 480, 528, and 912  $\mu\text{s}$ ), as well as the results of fitting performed based on the above-mentioned procedure, are shown in Fig. 4.

The subfigures in the upper row in Fig. 4 [i.e., Figs. 4(a), 4(c), 4(e), 4(g), and 4(i)] show the experimental results conditioned on  $|g\rangle$ , which are obtained using the pulse sequence in Fig. 1(b). Similarly, the subfigures in the lower row [Figs. 4(b), 4(d), 4(f), 4(h), and 4(j)] show those conditioned on  $|e\rangle$ , which are obtained using the pulse sequence in

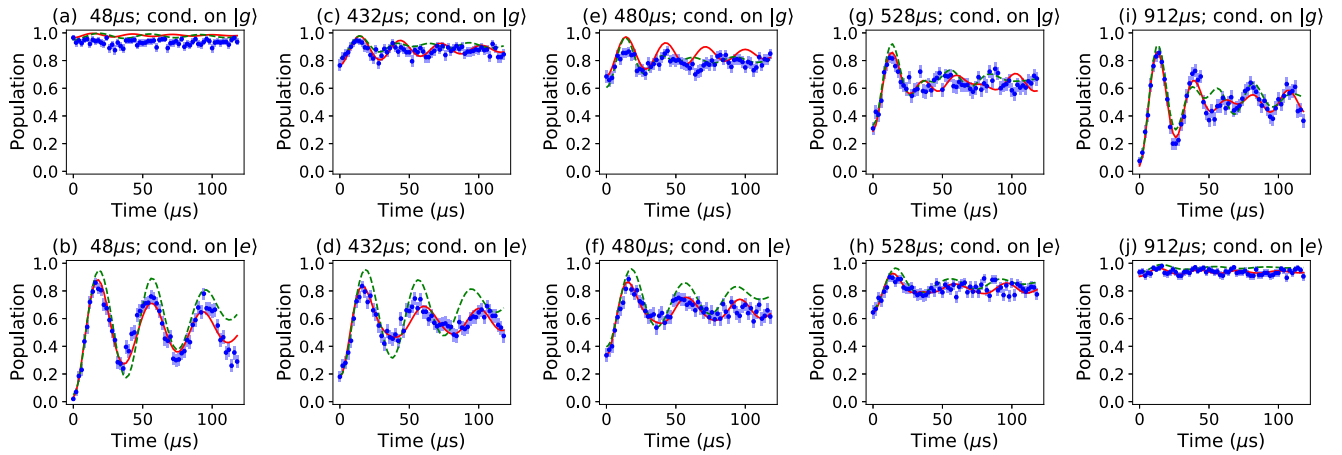


FIG. 4. BSB Rabi oscillations (blue points) obtained by truncating the quantum simulation (adiabatic transfer) and by illuminating using a square pulse with a variable duration. Here, only certain values for the duration of the quantum simulation are picked up. Each experimental point is the average of 100 experiments, and the error is calculated by assuming a binomial distribution. The results for the fitting of the Rabi-oscillation signals with model functions are also shown (red curves). For comparison, numerically simulated results based on the JCH model (i.e., those including the effect of phonon hopping) are shown as green dashed curves (see the main text for details). The durations for the quantum simulation (adiabatic transfer) are (a), (b) 48, (c), (d) 432, (e), (f) 480, (g), (h) 528, and (i), (j) 912  $\mu\text{s}$  from the first column to the fifth. The results in the upper row [(a), (c), (e), (g), and (i)] are taken from measurements conditioned on  $|g\rangle$ , and those in the lower row [(b), (d), (f), (h), and (j)] on  $|e\rangle$ .

Fig. 1(c). The results in the upper row reflect such populations as  $P_{g,0}$ ,  $P_{g,1}$ , or  $P_{g,2}$  for the original state before the conditional measurement, while those in the lower row reflects such populations as  $P_{e,0}$ ,  $P_{e,1}$ , or  $P_{e,2}$ .

In Fig. 4(a), the peak-to-peak amplitude of the Rabi oscillation conditioned on  $|g\rangle$  is shown to be  $\sim 5\%$ . This corresponds to the population remaining in  $|g\rangle$  at the start point of the Rabi oscillation. The rest of the population ( $\sim 95\%$ ) is shelved to the auxiliary state  $|a\rangle$ , and that corresponds to the large offset in the population. On the other hand, in Fig. 4(b), the peak-to-peak amplitude of the Rabi oscillation conditioned on  $|e\rangle$  is shown to be  $\sim 95\%$ . This corresponds to the population hidden in  $|a\rangle$  in Fig. 4(a).

In the upper row in Fig. 4, populations at  $t > 0$  are determined by BSB Rabi dynamics against the initial populations  $\{P_{g,0}, P_{g,1}, P_{g,2}, \dots\}$ , while in the lower row populations are determined by BSB Rabi dynamics against  $\{P_{e,0}, P_{e,1}, P_{e,2}, \dots\}$ , which are mapped to  $\{|g, 0\rangle, |g, 1\rangle, |g, 2\rangle, \dots\}$  in advance by the carrier  $\pi$  pulse.

By using the parameter values obtained in the fitting as shown in Fig. 4, values for the variances are obtained, which will be explained later in this section.

For reference, we also performed numerical simulations of the JCH dynamics for the composite sequence comprised of an adiabatic passage [which is similar to what is shown in Fig. 3(a), but is truncated at some point] and the successive illumination of a BSB square pulse. The simulated results during the latter are shown in Figs. 4(a)–4(j) as green dashed curves. The same conditions for numerical simulations as in Fig. 3(a) are used here again. Although there are certain quantitative discrepancies, we can confirm that the numerically simulated results reproduce the qualitative behaviors of the experimental results. We should note that this analysis is not that categorized as a fitting. In general, it is not straightforward to perform fitting of the BSB Rabi oscillation results using the

JCH model. A complete simulation of the JCH model requires the information of various correlations in the system at the initial time (especially those between motional modes that belong to different ions), while such information is lacking in the BSB Rabi oscillation results. Acquiring such information necessitates procedures similar to quantum state tomography, while it is not known to be scalable when the number of ions is increased.

Values for the variances and internal-state population estimated by processing the experimental Rabi oscillation results, as well as those obtained in a numerical simulation, are shown in Fig. 5. The atomic variance [blue circles with error bars and dashed curve in Fig. 5(a)] shows a peak in the center. In this region, the excitations of the system take the form of polaritons, each of which is the superposition of an internal excitation and a phonon. In this case, the internal-excitation number fluctuates, resulting in the appearance of a peak in the atomic variance. The phonon number variance [black circles with error bars and dashed curve in Fig. 5(b)] increases around the center of the sweep. This indicates the emergence of the phonon SF state. The total variance [red circles with error bars and dashed curve in Fig. 5(c)] follows a similar trend. The irregularly high experimental values ( $\sim 0.3$ ) at  $0 \mu\text{s}$  in Figs. 5(b) and 5(c) are considered to be artifacts due to technical imperfections [47].

In the numerically simulated results in Figs. 5(b) and 5(c), at the region after  $500 \mu\text{s}$ , oscillatory behavior with a period of  $\sim 150 \mu\text{s}$  is seen in both the phonon and total variances. This feature may have arisen from the diabaticity in the motional states. Since the total sweep time of  $960 \mu\text{s}$  is not sufficiently long compared with the hopping time constant (defined as the inverse of the hopping rate,  $\sim 260 \mu\text{s}$ ), the system does not completely adiabatically follow the ground states and additional phonon excitations may be generated. This effect may be relaxed by choosing a longer sweep time.

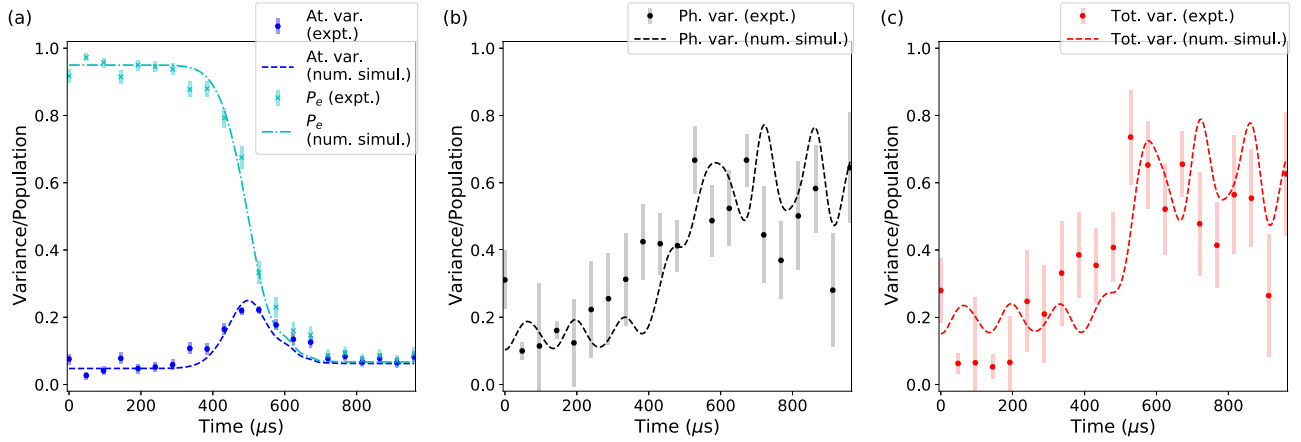


FIG. 5. (a) Atomic variance, excited-state population  $P_e$ , (b) phonon variance, and (c) total variance, which are obtained from an analysis involving the fitting of experimental results (points with error bars) and numerical simulation (dashed and dash-dotted curves).

We suppose that the relatively large fluctuations in the experimental phonon and total variances [Figs. 5(b) and 5(c)] observed in the region after 500  $\mu\text{s}$  have an origin related to this effect.

The internal-state population [cyan crosses with error bars and dash-dotted curve in Fig. 5(a)] shows a relatively smooth and solid transition. This indicates that adiabaticity of the internal states is satisfied. This experiment confirms that the method for conditional measurements described in this work, which is capable of measuring the internal and motional states simultaneously without mutual interference, is sufficient for investigating the quantum phase crossovers in the current system.

### VIII. DISCUSSION

The study of the ground-state properties in a JCH system, which can be dealt with by the conditional-measurement method in this work, may provide a basis for dynamical studies of the system as well as many-body quantum dynamics. The study of correlated particles such as polaritons may lead us toward more profound quantum mechanical properties or phenomena.

The conditional-measurement method described in this work can be applied to larger numbers of ions in a straightforward manner. By increasing the number of ions, a steep transition from one quantum phase to another is expected [48]. In a previous study using a Bose-particle system, a sudden change of quantum phases against parameter changes was observed [36]. The JCH system is expected to show a similar steep variation of quantum phases against parameter changes if an increased number of ions is used.

The fitting model functions used in this article assume that sideband Rabi oscillations are bound within the state manifold for each ion, and mutual interactions between ions are not considered. Although this assumption simplifies the analysis, it can lead to discrepancy between the experimental and fitted results. This discrepancy could be overcome if the full JCH model is used to obtain the fitting models in numerical simulations. However, this method of analysis is not considered to be scalable since the numerical simulation of the full JCH

model becomes increasingly difficult for larger numbers of ion sites and is effectively intractable [49]. In addition, fitting necessitates setting suitable initial values, which may allow arbitrariness to enter into the analysis process.

Another option that can overcome the shortcomings of using fitting for the analysis would be the use of discrete Fourier transforms. By not relying on fitting or numerical simulations of physical models to deduce phonon distributions, this method of analysis may be applied to larger numbers of ion sites with less difficulties and arbitrariness.

### IX. CONCLUSIONS

In conclusion, we proposed a scalable scheme for the simultaneous determination of internal and motional states in trapped ions based on conditional measurements. The scheme was applied to a system of polaritons in the JCH model, and a phase crossover was studied by evaluating the quantities such as the variance for the total excitation number (polariton number) per site. The scheme proposed here can be applied to larger JCH systems where steeper phase crossovers and transitions as well as nonequilibrium behaviors reflecting interactions are expected. In addition, the scheme can also be applied to other subjects in quantum simulations with trapped ions where both the internal and motional degrees of freedom are fully exploited as the simulation resources.

### ACKNOWLEDGMENTS

This article was supported by MEXT Quantum Leap Flagship Program (MEXT Q-LEAP) Grant No. JPMXS0118067477. R.O. was supported by JSPS KAKENHI Grant No. JP21J10054.

S.M. and R.O. contributed equally to this article.

### APPENDIX: ESTIMATION OF ERRORS IN THE EVALUATION OF VARIANCES

The errors in the evaluated values for the variances are calculated based on the propagation of errors using the partial derivatives of the variances with respect to certain quantities.



The squared error in the atomic variance [Eq. (8)] is obtained as

$$\begin{aligned} V[(\Delta\hat{N}_a)^2] &\simeq \left\{ \frac{\partial[(\Delta\hat{N}_a)^2]}{\partial P_e} \right\}^2 V(P_e) \\ &= (1 - 2P_e)^2 V(P_e). \end{aligned}$$

Here,  $V(X)$  represents the variance of a classical probabilistic variable  $X$ , which takes into account statistical fluctuations. This is contrasted with the variances in Eqs. (8)–(10), which are those of quantum observables that take into account both quantum and statistical fluctuations.  $V(P_e)$  is the variance of  $P_e$ , which is calculate as that of a binomial distribution based on the value of  $P_e$  and the number of samples.

Similarly, the squared error in the phonon variance [Eq. (9)] is calculated as

$$\begin{aligned} V[(\Delta\hat{N}_p)^2] &\simeq \sum_{n=0}^2 \left\{ \frac{\partial[(\Delta\hat{N}_p)^2]}{\partial P_n} \right\}^2 V(P_n) \\ &\quad + \sum_{k=0}^1 \sum_{l=k+1}^2 2 \frac{\partial^2[(\Delta\hat{N}_p)^2]}{\partial P_k \partial P_l} \text{Cov}(P_k, P_l) \\ &= \left\{ \frac{\partial[(\Delta\hat{N}_p)^2]}{\partial P_1} \right\}^2 V(P_1) + \left\{ \frac{\partial[(\Delta\hat{N}_p)^2]}{\partial P_2} \right\}^2 V(P_2) \\ &\quad + 2 \frac{\partial^2[(\Delta\hat{N}_p)^2]}{\partial P_1 \partial P_2} \text{Cov}(P_1, P_2) \\ &= (1 - 2P_1 - 4P_2)^2 V(P_1) + (4 - 4P_1 - 8P_2)^2 V(P_2) \\ &\quad + 2(-4) \text{Cov}(P_1, P_2). \end{aligned}$$

Here,  $\text{Cov}(P_1, P_2)$  represents the covariance of two classical probabilistic variables  $P_1$  and  $P_2$ . We use the relations  $P_1 = P_{g,1} + P_{e,1}$  and  $P_2 = P_{g,2} + P_{e,2}$ , and consider the fact that the two sets of variables,  $\{P_{g,0}, P_{g,1}, P_{g,2}\}$  and  $\{P_{e,0}, P_{e,1}, P_{e,2}\}$ , are determined, respectively, in separate experiments. There are constraints in the fitting process that the sum of the populations  $\{P_{g,0}, P_{g,1}, P_{g,2}\}$  or  $\{P_{e,0}, P_{e,1}, P_{e,2}\}$  matches  $P_g$  or  $P_e$ , respectively. Due to this, certain correlations (for example, between  $P_{g,1}$  and  $P_{g,2}$  or  $P_{e,1}$  and  $P_{e,2}$ ) arise. We take into account such correlations, while we do not take into account

other correlations. Thus, we assume

$$\begin{aligned} \text{Cov}(P_1, P_2) &\simeq \text{Cov}(P_{g,1}, P_{g,2}) + \text{Cov}(P_{e,1}, P_{e,2}), \\ V(P_1) &\simeq V(P_{g,1}) + V(P_{e,1}), \\ V(P_2) &\simeq V(P_{g,2}) + V(P_{e,2}). \end{aligned}$$

The quantities in the right-hand sides of these expressions are determined experimentally from the covariances and errors in the fitting process. If those quantities are substituted to the expression for  $V[(\Delta\hat{N}_p)^2]$ , the squared error in the phonon variance can be obtained.

The squared error in the total variance [Eq. (10)] can be calculated in a similar way,

$$\begin{aligned} V[(\Delta\hat{N}_t)^2] &= \left\{ \frac{\partial[(\Delta\hat{N}_p)^2]}{\partial P_e} \right\}^2 V(P_e) \\ &\quad + \left\{ \frac{\partial[(\Delta\hat{N}_p)^2]}{\partial P_{g,1}} \right\}^2 V(P_{g,1}) + \left\{ \frac{\partial[(\Delta\hat{N}_p)^2]}{\partial P_{e,1}} \right\}^2 V(P_{e,1}) \\ &\quad + \left\{ \frac{\partial[(\Delta\hat{N}_p)^2]}{\partial P_{g,2}} \right\}^2 V(P_{g,2}) + \left\{ \frac{\partial[(\Delta\hat{N}_p)^2]}{\partial P_{e,2}} \right\}^2 V(P_{e,2}) \\ &\quad + 2 \frac{\partial^2[(\Delta\hat{N}_p)^2]}{\partial P_{g,1} \partial P_{g,2}} \text{Cov}(P_{g,1}, P_{g,2}) \\ &\quad + 2 \frac{\partial^2[(\Delta\hat{N}_p)^2]}{\partial P_{e,1} \partial P_{e,2}} \text{Cov}(P_{e,1}, P_{e,2}) \\ &= [1 - 2P_e - 2(P_1 + 2P_2)]^2 V(P_e) \\ &\quad + (1 - 2P_1 - 4P_2 - 2P_e)^2 V(P_{g,1}) \\ &\quad + (1 - 2P_1 - 4P_2 + 2 - 2P_e)^2 V(P_{e,1}) \\ &\quad + (4 - 4P_1 - 8P_2 - 4P_e)^2 V(P_{g,2}) \\ &\quad + (4 - 4P_1 - 8P_2 + 4 - 4P_e)^2 V(P_{e,2}) \\ &\quad + 2(-4) \text{Cov}(P_{g,1}, P_{g,2}) + 2(-4) \text{Cov}(P_{e,1}, P_{e,2}). \end{aligned}$$

Here, again we only consider correlations arising in the process of fitting [ $\text{Cov}(P_{g,1}, P_{g,2})$ ,  $\text{Cov}(P_{e,1}, P_{e,2})$ ], and obtain the squared error in the total variance using the above relation.

- 
- [1] R. P. Feynman, Simulating physics with computers, *Intl. J. Theor. Phys.* **21**, 467 (1982).
- [2] R. Blatt and C. F. Roos, Quantum simulations with trapped ions, *Nat. Phys.* **8**, 277 (2012).
- [3] C. Monroe, W. C. Campbell, L.-M. Duan, Z.-X. Gong, A. V. Gorshkov, P. W. Hess, R. Islam, K. Kim, N. M. Linke, G. Pagano, P. Richerme, C. Senko, and N. Y. Yao, Programmable quantum simulations of spin systems with trapped ions, *Rev. Mod. Phys.* **93**, 025001 (2021).
- [4] E. T. Jaynes and F. W. Cummings, Comparison of quantum and semiclassical radiation theories with application to the beam maser, *Proc. IEEE* **51**, 89 (1963).
- [5] A. D. Greentree, C. Tahan, J. H. Cole, and L. C. L. Hollenberg, Quantum phase transitions of light, *Nat. Phys.* **2**, 856 (2006).
- [6] M. J. Hartmann, F. Brandao, and M. B. Plenio, Strongly interacting polaritons in coupled arrays of cavities, *Nat. Phys.* **2**, 849 (2006).
- [7] D. G. Angelakis, M. F. Santos, and S. Bose, Photon-blockade-induced Mott transitions and XY spin models in coupled cavity arrays, *Phys. Rev. A* **76**, 031805(R) (2007).
- [8] M. J. Hartmann, F. Brandao, and M. B. Plenio, Quantum many-body phenomena in coupled cavity arrays, *Laser Photon. Rev.* **2**, 527 (2008).

- [9] M. Hohenadler, M. Aichhorn, L. Pollet, and S. Schmidt, Polariton Mott insulator with trapped ions or circuit QED, *Phys. Rev. A* **85**, 013810 (2012).
- [10] M. Gessner, F. Schlawin, and A. Buchleitner, Probing polariton dynamics in trapped ions with phase-coherent two-dimensional spectroscopy, *J. Chem. Phys.* **142**, 212439 (2015).
- [11] M. J. Hartmann, Quantum simulation with interacting photons, *J. Opt.* **18**, 104005 (2016).
- [12] D. E. Chang, J. S. Douglas, A. Gonzalez-Tudela, C. L. Hung, and H. J. Kimble, Colloquium: Quantum matter built from nanoscopic lattices of atoms and photons, *Rev. Mod. Phys.* **90**, 031002 (2018).
- [13] S. Kato, N. Nemet, K. Senga, S. Mizukami, X. Huang, S. Parkins, and T. Aoki, Observation of dressed states of distant atoms with delocalized photons in coupled-cavities quantum electrodynamics, *Nat. Commun.* **10**, 1160 (2019).
- [14] A. J. Hoffman, S. J. Srinivasan, S. Schmidt, L. Spietz, J. Aumentado, H. E. Türeci, and A. A. Houck, Dispersive Photon Blockade in a Superconducting Circuit, *Phys. Rev. Lett.* **107**, 053602 (2011).
- [15] A. A. Houck, H. E. Türeci, and J. Koch, On-chip quantum simulation with superconducting circuits, *Nat. Phys.* **8**, 292 (2012).
- [16] S. Schmidt and J. Koch, Circuit QED lattices: Towards quantum simulation with superconducting circuits, *Ann. Phys.* **525**, 395 (2013).
- [17] J. Raftery, D. Sadri, S. Schmidt, H. E. Türeci, and A. A. Houck, Observation of a Dissipation-Induced Classical to Quantum Transition, *Phys. Rev. X* **4**, 031043 (2014).
- [18] M. Fitzpatrick, N. M. Sundaesan, A. C. Y. Li, J. Koch, and A. A. Houck, Observation of a Dissipative Phase Transition in a One-Dimensional Circuit QED Lattice, *Phys. Rev. X* **7**, 011016 (2017).
- [19] P. A. Ivanov, S. S. Ivanov, N. V. Vitanov, A. Mering, M. Fleischhauer, and K. Singer, Simulation of a quantum phase transition of polaritons with trapped ions, *Phys. Rev. A* **80**, 060301(R) (2009).
- [20] K. Toyoda, Y. Matsuno, A. Noguchi, S. Haze, and S. Urabe, Experimental Realization of a Quantum Phase Transition of Polaritonic Excitation, *Phys. Rev. Lett.* **111**, 160501 (2013).
- [21] S. Debnath, N. M. Linke, S.-T. Wang, C. Figgatt, K. A. Landsman, L.-M. Duan, and C. Monroe, Observation of Hopping and Blockade of Bosons in a Trapped Ion Spin Chain, *Phys. Rev. Lett.* **120**, 073001 (2018).
- [22] R. Ohira, S. Kume, K. Takayama, S. Muralidharan, H. Takahashi, and K. Toyoda, Blockade of phonon hopping in trapped ions in the presence of multiple local phonons, *Phys. Rev. A* **103**, 012612 (2021).
- [23] R. Ohira, S. Kume, H. Takahashi, and K. Toyoda, Polariton blockade in the Jaynes-Cummings-Hubbard model with trapped ions, *Quantum Sci. Technol.* **6**, 024015 (2021).
- [24] D. Porras and J. I. Cirac, Bose-Einstein Condensation and Strong-Correlation Behavior of Phonons in Ion Traps, *Phys. Rev. Lett.* **93**, 263602 (2004).
- [25] K. R. Brown, C. Ospelkaus, Y. Colombe, A. C. Wilson, D. Leibfried, and D. J. Wineland, Coupled quantized mechanical oscillators, *Nature (London)* **471**, 196 (2011).
- [26] M. Harlander, R. Lechner, M. Brownnutt, R. Blatt, and W. Hänsel, Trapped-ion antennae for the transmission of quantum information, *Nature (London)* **471**, 200 (2011).
- [27] S. Haze, Y. Tateishi, A. Noguchi, K. Toyoda, and S. Urabe, Observation of phonon hopping in radial vibrational modes of trapped ions, *Phys. Rev. A* **85**, 031401(R) (2012).
- [28] A. C. Wilson, Y. Colombe, K. R. Brown, E. Knill, D. Leibfried, and D. J. Wineland, Tunable spin-spin interactions and entanglement of ions in separate potential wells, *Nature (London)* **512**, 57 (2014).
- [29] K. Toyoda, R. Hiji, A. Noguchi, and S. Urabe, Hong-Ou-Mandel interference of two phonons in trapped ions, *Nature (London)* **527**, 74 (2015).
- [30] M. Tamura, T. Mukaiyama, and K. Toyoda, Quantum Walks of a Phonon in Trapped Ions, *Phys. Rev. Lett.* **124**, 200501 (2020).
- [31] R. Ohira, T. Mukaiyama, and K. Toyoda, Phonon-number-resolving detection of multiple local phonon modes in trapped ions, *Phys. Rev. A* **100**, 060301(R) (2019).
- [32] S. X. Wang, J. Labaziewicz, Y. Ge, R. Shewmon, and I. L. Chuang, Demonstration of a quantum logic gate in a cryogenic surface-electrode ion trap, *Phys. Rev. A* **81**, 062332 (2010).
- [33] N. V. Vitanov, T. Halfmann, B. W. Shore, and K. Bergmann, Laser-induced population transfer by adiabatic passage technique, *Annu. Rev. Phys. Chem.* **52**, 763 (2001).
- [34] E. K. Irish, C. D. Ogden, and M. S. Kim, Polaritonic characteristics of insulator and superfluid states in a coupled-cavity array, *Phys. Rev. A* **77**, 033801 (2008).
- [35] D. Jaksch, C. Bruder, J. I. Cirac, C. W. Gardiner, and P. Zoller, Cold Bosonic Atoms in Optical Lattices, *Phys. Rev. Lett.* **81**, 3108 (1998).
- [36] M. Greiner, O. Mandel, T. Esslinger, T. W. Hansch, and I. Bloch, Quantum phase transition from a superfluid to a Mott insulator in a gas of ultracold atoms, *Nature (London)* **415**, 39 (2002).
- [37] X. L. Deng, D. Porras, and J. I. Cirac, Quantum phases of interacting phonons in ion traps, *Phys. Rev. A* **77**, 033403 (2008).
- [38] D. J. Wineland, C. Monroe, W. M. Itano, D. Leibfried, B. E. King, and D. M. Meekhof, Experimental issues in coherent quantum-state manipulation of trapped atomic ions, *J. Res. Natl. Inst. Stand. Technol.* **103**, 259 (1998).
- [39] M. Šašura and V. Bužek, Cold trapped ions as quantum information processors, *J. Mod. Opt.* **49**, 1593 (2002).
- [40] K. G. Johnson, J. D. Wong-Campos, A. Restelli, K. A. Landsman, B. Neyenhuis, J. Mizrahi, and C. Monroe, Active stabilization of ion trap radio frequency potentials, *Rev. Sci. Instrum.* **87**, 053110 (2016).
- [41] D. Manzano, A short introduction to the Lindblad master equation, *AIP Adv.* **10**, 025106 (2020).
- [42] The cause of the reduction by 5% in the population of  $|e\rangle$  can be explained as being due to the incomplete preparation of the atomic MI state by the carrier  $\pi$  pulse. We use the individual illumination of each ion with a dedicated beam at 729 nm. Each beam is passed through a dedicated polarization-maintaining optical fiber to assure path stability. However, this fiber may produce a drift in the optical phases. Fluctuations in interference between the beams caused by this drift of optical phases, as well as those in the pointing of the beams, lead to relatively large intensity fluctuations at the positions of the ions and affect the fidelity of rotations even for the carrier transition.
- [43] D. M. Meekhof, C. Monroe, B. E. King, W. M. Itano, and D. J. Wineland, Generation of Nonclassical Motional States of a Trapped Atom, *Phys. Rev. Lett.* **76**, 1796 (1996).

- [44] In principle, the previously quoted transverse-relaxation rate  $\gamma_T$  in the Lindblad master equation and this  $\gamma_R$  should have a certain relation. If the latter is assumed to be determined purely from the former,  $\gamma_R \sim 0.25 \times \gamma_T$  is expected, which is confirmed by numerical simulations. In that case,  $\gamma_R \sim 0.05$  kHz is expected if  $\gamma_T \sim 2\pi \times 0.19$  kHz is satisfied. On the other hand, the actual value of  $\gamma_R$  determined from the chi-square minimization, as explained in Sec. VII A, is  $2\pi \times 1.1$  kHz, which is more than an order of magnitude larger than the above-mentioned value. This discrepancy may be explained by the concrete nature of the fluctuations. If an adiabatic-transfer process such as that in Fig. 3(a) is used and the typical timescale for the fluctuations is much longer than the pulse duration, the adiabatic transfer process is not affected significantly by the fluctuations thanks to their robustness against parameter variations. This may be why the assumed relaxation rate that matches the experimental results is much smaller than that for the numerical simulation results shown in Fig. 3(a).
- [45] The factors that may make this assumption invalid are the residual phonon number after sideband cooling (estimated to be  $\sim 0.2$  in the present case), heating during adiabatic transfer ( $\sim 5 \times 10^{-3}$  quanta), and off-resonance excitation of the carrier transition by the red-sideband optical pulse for the adiabatic transfer ( $< 0.03$ ). Here, we ignore their effects.
- [46] Here, for simplicity, we assume that the errors are symmetric for the positive and negative directions, and nonlinear dependences of the deviations around the estimated values are ignored. This could lead to the appearance of unphysical values for the bounds of the confidence intervals: The negative values in Figs. 5(a) and 5(b) at 96 and 192  $\mu$ s are considered to be due to this.
- [47] We suppose that the discrepancy between the experimental variances and those from numerical simulations at 0  $\mu$ s was caused by the thermal effects of an acousto-optic modulator (AOM) used in the experiment. In our apparatus, a double-pass AOM system was used for switching and frequency shift of 729-nm beams. The AOM was completely turned off (i.e., with a 0% duty cycle) when a measurement was not performed, and it was turned on with a finite duty cycle when a measurement was started. We speculated that the difference between these duty cycles caused a transient behavior in the thermal effects of the AOM when a measurement was started, resulting in a drift of the output power. Since the final temperature achieved in sideband cooling depends on the power of the cooling laser beam, a sufficient cooling may not be obtained if the optical power is not at the optimum condition. We speculated that such a nonoptimum power in sideband cooling resulted in a rise of the initial temperature for the quantum simulation and a resulting increase of the phonon and total variances at the time of 0  $\mu$ s.
- [48] R. Islam, E. E. Edwards, K. Kim, S. Korenblit, C. Noh, H. Carmichael, G. D. Lin, L.-M. Duan, C. C. Joseph Wang, J. K. Freericks, and C. Monroe, Onset of a quantum phase transitions with a trapped ion quantum simulator, *Nat. Commun.* **2**, 377 (2011).
- [49] In our estimation, numerical simulation using the full JCH model with more than 17 ion sites and the commensurate filling of one excitation per ion site requires memory that can hold a number of basis states as large as that in a 40-spin system and cannot be easily solved with existing classical computers.